Inorganic Chemistry

pubs.acs.org/IC Article

Silver-π Interaction: A Diverse Approach to Hybrid Material and Its Efficacy in Electrocatalytic Reduction of Nitrate to Ammonia

Calvin Samuel, Gujju Narsimhulu, Garima Bangar, Sai Hemanth Kumar Dasari, Gopalan Rajaraman,* and Viswanathan Baskar*

Cite This: *Inorg. Chem.* 2024, 63, 21670−21678 Read Online

ACCESS | Metrics & More | Article Recommendations | Supporting Information

ABSTRACT: Inspired by the intriguing nature of the metal-π interaction in organometallic chemistry, a novel 1D hybrid material has been designed. Herein, a functionalized tellurium allyl macrocycle (TAM) acts as a molecular building block and is knit together via silver-π interaction to obtain Ag-TAM. Ag is coordinated to two allyl groups and a phenyl ring in η^2 mode. Instead of the conventional polymerization strategy, a metal-π interaction is employed to interlink macrocycles. TAM and Ag-TAM showed electrocatalytic capability for the conversion of nitrate to ammonia. Ag-TAM showed an NH_3 yield rate 2-fold greater than TAM with a high faradaic efficiency of 94.6% with good durability, proving that interlinking of macrocycles via metal-π interaction improves the catalytic activity. Detailed periodic density functional theory (DFT) calculations unveil novel mechanistic insights, suggesting cooperative catalysis between neighboring Ag sites and contributing to the enhanced efficiency.

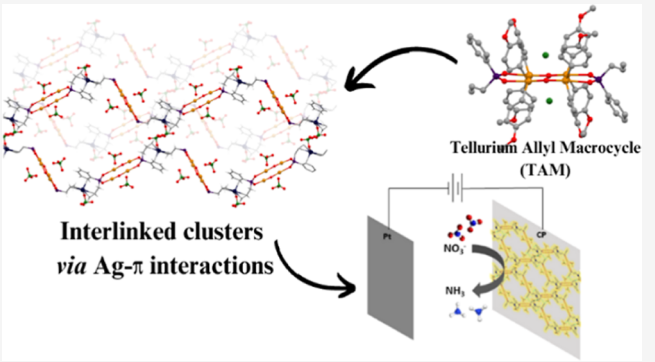

INTRODUCTION

Ammonia is vital in catering to the global demand for agricultural products in a world of increasing population. Conventionally, ammonia is produced by the Haber−Bosch process in which N_2 from the air is reacted with H_2 at very high temperature and high pressure.[1] This accounts for 1−2% of global energy consumption and generates an enormous amount of CO_2. In the last few decades, researchers have developed alternate strategies like electrochemical reduction of nitrogen to ammonia[2] to tackle this issue, but they have their own shortcomings.[3] In recent times, the electrochemical reduction of nitrate (NO_3^-) to ammonia (ERNA) has garnered a lot of attention, especially as it converts NO_3^-, a common water pollutant as a result of anthropogenic activities, to useful ammonia.[4] The accretion of nitrate potentially causes acid rain, photochemical smog, and various health issues.[5] Therefore, it is highly desirable to transform NO_3^- into valuable products. A variety of metals[6−10] and materials[11−20] have shown significant ERNA activity, with hybrid materials,[21−24] one among them.

Hybrid materials are materials wherein two different components are synergistically combined to achieve a far superior material.[25,26] Different categories include inorganic−organic, organometallic−organic,[27−29] and organometallic−inorganic hybrid materials.[30−32] Over the last few decades, there has been tremendous growth in the field of inorganic−organic hybrid materials with the advent of sol−gel-based hybrid materials, metal−organic framework (MOFs), coordination polymers (CPs), cross-linked cluster-based hybrid materials, etc. These hybrid materials have shown vital applications in the field of gas adsorption,[33,34] molecular sensing,[35,36] separation,[37,38] electrochromism,[39] and catalysis,[40] to name a few. Various types of bonding/interactions such as ionic, covalent, coordination, H-bonding, and van der Waals have been employed to obtain these materials. MOFs and CPs are typically built by organic linkers having N and O donor atoms forming covalent bonds with the metal, while conventionally cross-linked cluster-based hybrid materials are produced by copolymerizing preformed functionalized clusters with an organic copolymer. One distinction of cross-linked clusters is that these clusters act as molecular building blocks and do not lose their original molecular identity. On the other hand, hybrid materials having organometallic components have not seen the same meteoric rise.

In organometallics, a classic interaction is the metal-π interaction. The metal-π interaction has been prominent for several applications, especially in catalysis.[41−46] Over the years,

Received: June 21, 2024
Revised: August 9, 2024
Accepted: August 29, 2024
Published: September 3, 2024

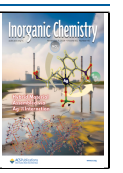

https://doi.org/10.1021/acs.inorgchem.4c02578
Inorg. Chem. 2024, 63, 21670−21678

these interactions have led to exciting moieties, such as an unusual silver-aromatic interaction wherein η^3-phenyl ring links led to a 3D metal−organic framework.[47] This was the first example of an unusual π-interaction being used to link coordination sheets. The advent of Ln-based sandwich and multidecker compounds resulted in the increase of energy barrier as well as blocking temperatures in single molecular magnetism (SMM).[48−53] Recently, Hatano et al. isolated polyarene Pd cluster, which was stabilized by neutral six-membered arene rings via face-capping coordination,[54] and few research groups have developed cyclic oligomers/sandwich-type materials.[55,56] So, the relevance of this class of interaction has not waned off, and boundaries are being expanded on a regular basis. Along this line, imagining a novel cross-linked or interlinked cluster-based hybrid material born from metal-π interaction instead of the conventional strategy is enticing.

Our research group has been interested in organotellurium chemistry[57,58] and has explored macrocycles with secondary interactions.[59] Here, we report a tellurium allyl macrocycle (TAM), a 12-membered tellurium macrocycle incorporated with a functionalized phosphinate. TAM functions as a molecular building block and interacts with silver to expand to a 1D interlinked chain, Ag-TAM, wherein silver acts as a linker via a silver-π interaction. We have also investigated TAM and Ag-TAM potential as electrocatalysts for electrocatalytic reduction of nitrate to ammonia and observed the enhancement of its activity with the interlinking of the macrocycles.

EXPERIMENTAL SECTION

Instrumentation. Infrared spectra were recorded by using a Nicolet iS5 FTIR spectrometer. ESI-MS spectra were recorded using a Bruker MaXis HRMS (ESI-TOF analyzer) equipment. NMR spectra were recorded on Bruker Avance-400 and 500 MHz FT NMR spectrometers at room temperature. Single-crystal X-ray diffraction (SCXRD) data collection for TAM was carried out at 100 K and for Ag-TAM at room temperature with an XtaLAB Synergy, a single source at offset/far, HyPix3000 diffractometer, and a Rigaku Oxford HyPix3000 CCD plate detector system [λ (Mo Kα) = 0.71073 Å] with a mirror monochromator. The data were reduced using CrysAlisPro version 1.171.40.35a (Rigaku OD, 2018). The structures were solved using SHELXT and refined using SHELXL-2018/3 in Olex2 1.3-ac4 software.[60−62] All non-hydrogen atoms were refined anisotropically. In Ag-TAM, the disorder containing oxygen attached to silver and chlorine was constrained using EADP, and C1 and C2 were restrained using the DFIX instructions in SHELXL-2018/3. In the crystal structure of Ag-TAM, the voids contained disordered solvents. The OLEX2 solvent mask routine (similar to PLATON/SQUEEZE) was used to mask out the disordered electron density. A solvent mask was calculated, and 119 electrons were found in a volume of 925\Å^3 in 2 voids per unit cell. This is consistent with the presence of 1.5[C_6H_6] per asymmetric unit, which accounts for 126 electrons per unit cell. Powder X-ray diffraction (PXRD) patterns were collected over the 2θ range of 5−50° at a scan rate of 3.9°/min. Field emission-scanning electron microscopy (FESEM) imaging, energy-dispersive spectroscopy (EDS), and elemental mapping were studied using an Ultra 55 Carl Zeiss instrument. High-resolution transmission electron microscopy (HR-TEM) was studied using a Jeol JEM-F200 instrument. X-ray photoelectron spectroscopy (XPS) spectra were collected with a Thermo Scientific K-ALPHA surface analysis spectrometer using Al Kα radiation (1486.6 eV). For elemental analysis, an ICP-OES Agilent-5800 instrument was used. TGA was recorded with a PerkinElmer STA 8000 thermogravimetric analyzer under a nitrogen gas flow rate of 20 mL/min and a heating rate of 10 °C/min. Graphics of the crystal structures were generated with Mercury.

Reagents and General Procedures. Phenyl allyl phosphinic acid[63] and bis(*p*-methoxyphenyl) tellurium dichloride[64] were synthesized according to literature reports. Phenyl phosphinic acid, $TeCl_4$, and $AgClO_4.xH_2O$ were purchased from Sigma-Aldrich; Na_2SO_4, KNO_3, and benzene were purchased from Finar, while allyl bromide and anisole were purchased from Avra. All solvents and reagents were purified before use by adopting standard methods.

Synthesis of TAM. In a 50 mL round-bottom flask, phenyl allyl phosphinic acid (0.07 g, 0.3876 mmol) was dissolved in 10 mL of benzene, followed by the addition of triethylamine (0.12 mL, 0.861 mmol). After stirring for 5 min, bis(*p*-methoxyphenyl) tellurium dichloride (0.32 g, 0.7752 mmol) was added, and the mixture was stirred at room temperature for 24 h. Afterward, the mixture was filtered, and colorless, hexagon-shaped crystals were grown from the mother liquor by slow evaporation for 4-5 days. Yield: 0.17 g (96%). IR: 3062.40 (w), 3011.20 (w), 2939.28 (w), 2834.02 (w), 1585.22 (s), 1568.14 (s), 1492.90 (s), 1458.63 (s), 1437.37 (s), 1401.21 (m), 1290.61 (s), 1246.99 (s), 1174.64 (s), 1109.60 (s), 1068.29 (m), 1006.18 (s), 910.48 (m), 824.05 (s), 789.11 (s), 746.76 (m), 694.52 (m), 665.41 (s), 610.01 (m), 590.01 (m), 505.83 (s), 470.43 (m), 450.02 (s).

Synthesis of Ag-TAM. TAM (100 mg, 0.054 mmol) and $AgClO_4.xH_2O$ (91 mg, 0.432 mmol) were transferred to a 50 mL round-bottom flask covered in aluminum foil in a glovebox and sealed with a rubber septum. Then, 20 mL of benzene was introduced through a syringe, and the mixture was stirred at room temperature for 12 h. Afterward, the mixture was filtered, and the solvent was removed in vacuo, leaving an oily residue. The residue was dissolved in benzene/chloroform/dichloromethane in a 1:1:1 ratio, and hexane was diffused onto it to obtain colorless, block-shaped crystals. IR: 3100.79 (w), 3072.40 (w), 2940.14 (w), 2839.21 (m), 1583.37 (s), 1491.11 (s), 1459.63 (s), 1438.94 (m), 1403.28 (m), 1295.45 (s), 1250.74 (s), 1176.97 (s), 1094.38 (s), 1058.29 (m), 1008.84 (s), 926.21 (s), 821.45 (s), 789.15 (s), 752.29 (m), 645.25 (s), 617.72 (s), 590.91 (m), 514.55 (s), 505.83 (s), 475.45 (s), 444.05 (s).

Electrochemical NRA Measurements. Electrochemical nitrate reduction was carried out in a CHI6112E electrochemical workstation using a three-electrode system (working electrode—carbon paper coated with TAM/Ag-TAM, counter electrode—Pt wire, and reference electrode—Ag/AgCl) and an H-type electrolytic cell separated by the Nafion membrane at room temperature. Na_2SO_4 solution (0.5 M, 126 mL) was evenly distributed to the cathode and anode compartments as an electrolyte. 0.05 M KNO_3 was added into the cathode compartment for NO_3^- reduction. Catalyst ink was prepared by dispersing 5 mg of TAM or Ag-TAM in 800 μL of ethanol/water (4:1) and 200 μL of Nafion, followed by sonication for 30 min. Afterward, a 1 cm × 0.5 cm carbon paper was coated with 200 μL of catalyst and dried overnight in an oven at 50 °C.

Initially, linear sweep voltammetry (LSV) was conducted for TAM and Ag-TAM with an external NO_3^- source at a rate of 5 mVs^{-1} from 0.2 to −1.9 V vs Ag/AgCl (0.8 to −1.28 V vs reversible hydrogen electrode (RHE)). After the addition of NO_3^-, the current increased significantly, showing the interaction of nitrate with the working electrode. The potentiostatic test was carried out at different potentials for 3 h at a stirring rate of 300 rpm. All potentials were recorded against the RHE.

Isotope Labeling Experiment. The isotope labeling experiment was carried out by adopting a literature method.[65] $K^{15}NO_3$ (98 atom %) with a concentration of 0.01 M was used as the feeding N-source to clarify the source of ammonia. After electrochemical reduction, 525 μL of electrolyte was mixed with 50 μL of 0.5 M H_2SO_4, 50 μL of DMSO-d_6, 25 μL of 12.5 mM maleic acid, and 25 μL of 27 mM Gd^{3+}, followed by collection of ^{1}H NMR data.

Computational Details. All of the density functional theory (DFT) calculations were performed via the Vienna Ab initio Software Package (VASP 6.2.1) code within the Perdew−Burke−Ernzerhof (PBE) generalized gradient approximation and the projected augmented wave (PAW) method. The cutoff energy for the plane-wave basis set was set to 400 eV, while the Brillouin zone was sampled at the Gamma point. Convergence thresholds were set to 10^{-4} eV for

https://doi.org/10.1021/acs.inorgchem.4c02578
Inorg. Chem. 2024, 63, 21670−21678

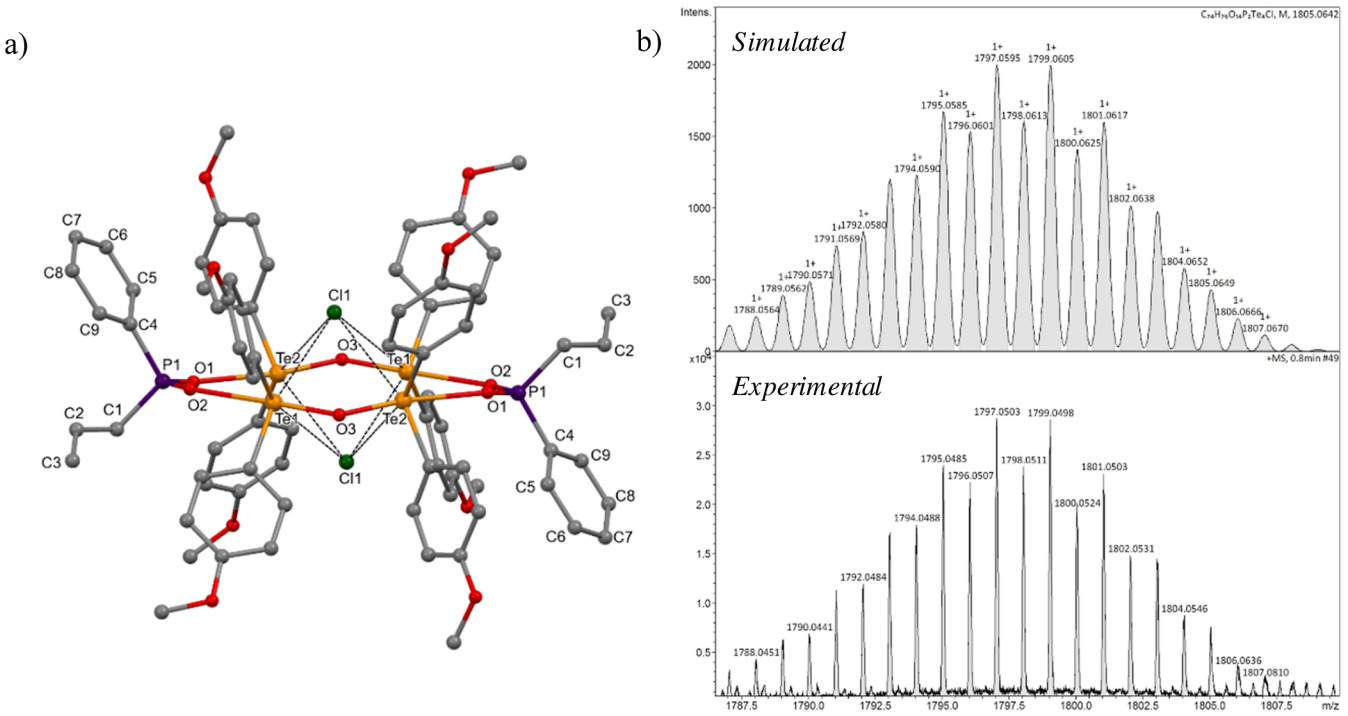

Figure 1. (a) Structure of TAM. Hydrogens and benzene solvate are omitted for clarity (orange−Te, purple−P, green−Cl, red−O, gray−C). (b) ESI-MS of TAM.

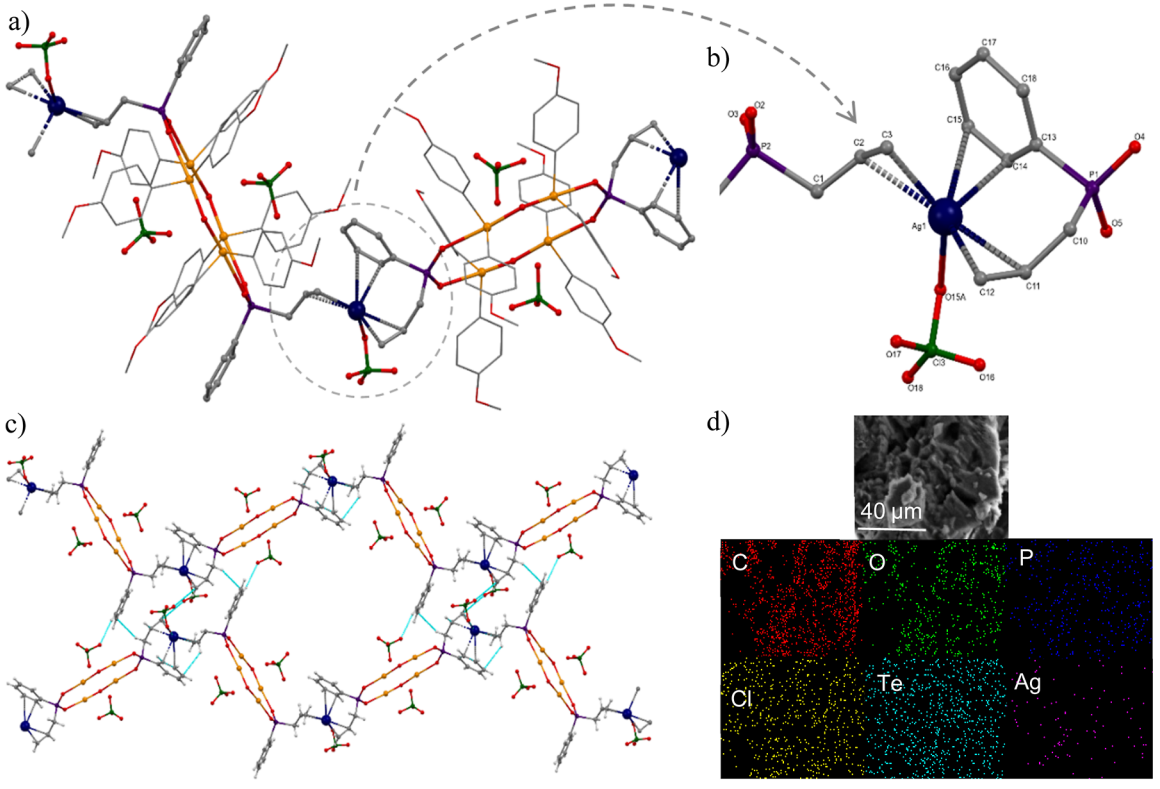

Figure 2. (a) Structure of Ag-TAM. Hydrogens are omitted for clarity (Prussian blue−Ag, orange−Te, purple−P, green−Cl, red−O, gray−C). (b) Coordination mode of silver in Ag-TAM. (c) Pseudo 3D structure of Ag-TAM through weak interactions (denoted by cyan lines). (d) Elemental mapping of Ag-TAM.

the energy and to 0.01 eV/Å for the forces. The convergence criterion for the electronic self-consistent iteration and force was set to 10^{-5} eV and 0.01 eV/Å, respectively, with a 1 × 1 × 1 Gamma-Pack *k*-point mesh.

RESULTS AND DISCUSSION

First, TAM was synthesized by reacting phenyl allyl phosphinic acid with R_2TeCl_2 [R = *p*-methoxyphenyl] in benzene at room temperature using triethylamine as a base. Colorless crystals of

https://doi.org/10.1021/acs.inorgchem.4c02578
Inorg. Chem. 2024, 63, 21670−21678

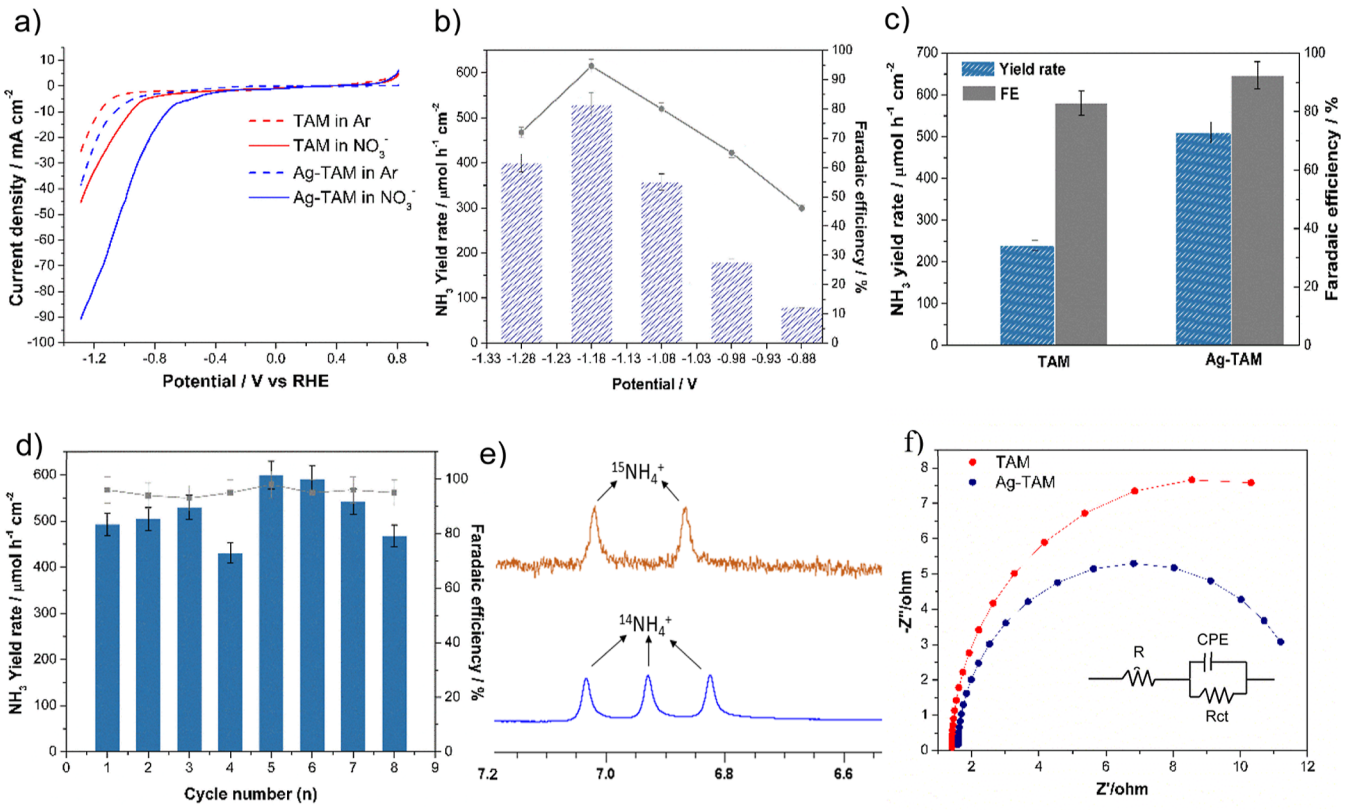

Figure 3. (a) LSV curves of TAM and Ag-TAM in 0.5 M Na_2SO_4 with and without NO_3^-. (b) Potential-dependent NH_3 yield rate and faradaic efficiency over Ag-TAM. (c) NH_3 yield rate and faradaic efficiency over TAM and Ag-TAM, respectively. (d) Recyclability test at −1.18 V over the Ag-TAM cathode. (e) ^1H NMR spectrum of products after ERNA using $^{14}NO_3^-$ and $^{15}NO_3^-$ at −1.18 V. (f) Nyquist plot for TAM and Ag-TAM in 0.5 M Na_2SO_4. Inset: the equivalent circuit for fitting data.

TAM were obtained by the slow evaporation of the mother liquor. Structural analysis showed that TAM crystallized in triclinic space group $P\bar{1}$ with half of the molecule in the asymmetric unit. It comprises two ditelluroxane units bridged by a phosphinate on either side with chloride above and below the macrocycle (Figure 1a). The macrocyclic core is dicationic, and the chlorides, held by secondary interactions, balance the charge. TAM is functionalized with phosphinates containing phenyl and allyl groups. C1−C2 and C2−C3 in the allyl group have bond distances of 1.493 and 1.312 Å, respectively, while the allyl and phenyl groups (C4−P1−C1) make an angle of 107.12° (crystallographic information in ESI). $^{31}P\{^1H\}$ NMR gives a singlet at δ 26.5 ppm (Figure S4), while ESI-MS revealed an m/z peak at 1797.0503 (Figure 1b), which corresponds to $[\{((p\text{-}OMeC_6H_4)_2Te)_2O(Ph(C_3H_5)\text{-}PO_2)\}_2\{Cl\}]^+$ formed by loss of chloride. This also shows that the structure is quite stable in the solution state. Additionally, the phase purity of crystalline TAM was confirmed by powder X-ray diffraction (PXRD), which is identical to the simulated pattern from SCXRD data (Figure S5), and thermogravimetric analysis (TGA) showed that the structure is stable until 200 °C, after which there is a gradual loss of weight (Figure S6).

Having prepared the building block, we proceeded to synthesize the hybrid material. TAM reacts with $AgClO_4.xH_2O$ in benzene at room temperature in a N_2 atmosphere to produce Ag-TAM, where TAM molecules are knitted together by silver. Structural analysis showed that Ag-TAM crystallized in the triclinic space group $P\bar{1}$ wherein the asymmetric unit consists of two half units of macrocycles coordinated to $AgClO_4$. Here, Ag acts as a linker with $AgClO_4$ held by phenyl and allyl groups from one macrocycle and the allyl group from another macrocycle via metal-π bonding in η^2: η^2: η^2 mode to give rise to an interlinked 1D macrocycle (Figure 2a). The macrocycles are arranged in a zigzag fashion, with their planes almost perpendicular to each other, making an angle of 88.4° (Figure S14). The capping chloride in TAM is replaced by perchlorate in the case of Ag-TAM. Ag is four-coordinated with two allyl groups, one phenyl ring, and one perchlorate (Figure 2b). The Ag atom coordinates with both the allyl groups in an η^2 fashion with bond distances of 2.483 Å (Ag1−C2), 2.421 Å (Ag1−C3), 2.527 Å (Ag1−C11), and 2.381 Å (Ag1−C12). Similarly, Ag coordinates to the phenyl ring in an η^2 fashion with bond distances of 2.717 Å (Ag1−C14) and 3.18 Å (Ag1−C15). The C═C bond in the allyl groups shows bond distances of 1.337 Å (C2−C3) and 1.343 Å (C11−C12), which shows slight lengthening of the bonds when compared to free allyl in TAM. ^1H NMR showed two doublets at δ 4.8 and 4.9 ppm and a multiplet at δ 5.5 ppm, corresponding to allylic hydrogens (Figure S15). This and the bond lengths show that the carbons coordinated to Ag stay in the sp^2 hybridization. The angle between the allyl and phenyl groups is 106.93° (C10−P1−C13) on one side, which is similar to TAM, while on the other side, it makes an angle of 101.88° (C1−P2−C4), which is a slight decrease. Moreover, the adjacent chains in Ag-TAM are cross-linked via weak interchain C12···O17−Cl3 (C12···O17 = 3.005 Å), C7···H10A-C10 (C7···H10A = 2.726 Å), Cl1−O13···H8−C8 (O13···H8 = 2.887 Å) interaction and H-bonds to form a pseudo-3D arrangement (Figure 2c). $^{31}P\{^1H\}$ NMR shows a

https://doi.org/10.1021/acs.inorgchem.4c02578
Inorg. Chem. 2024, 63, 21670−21678

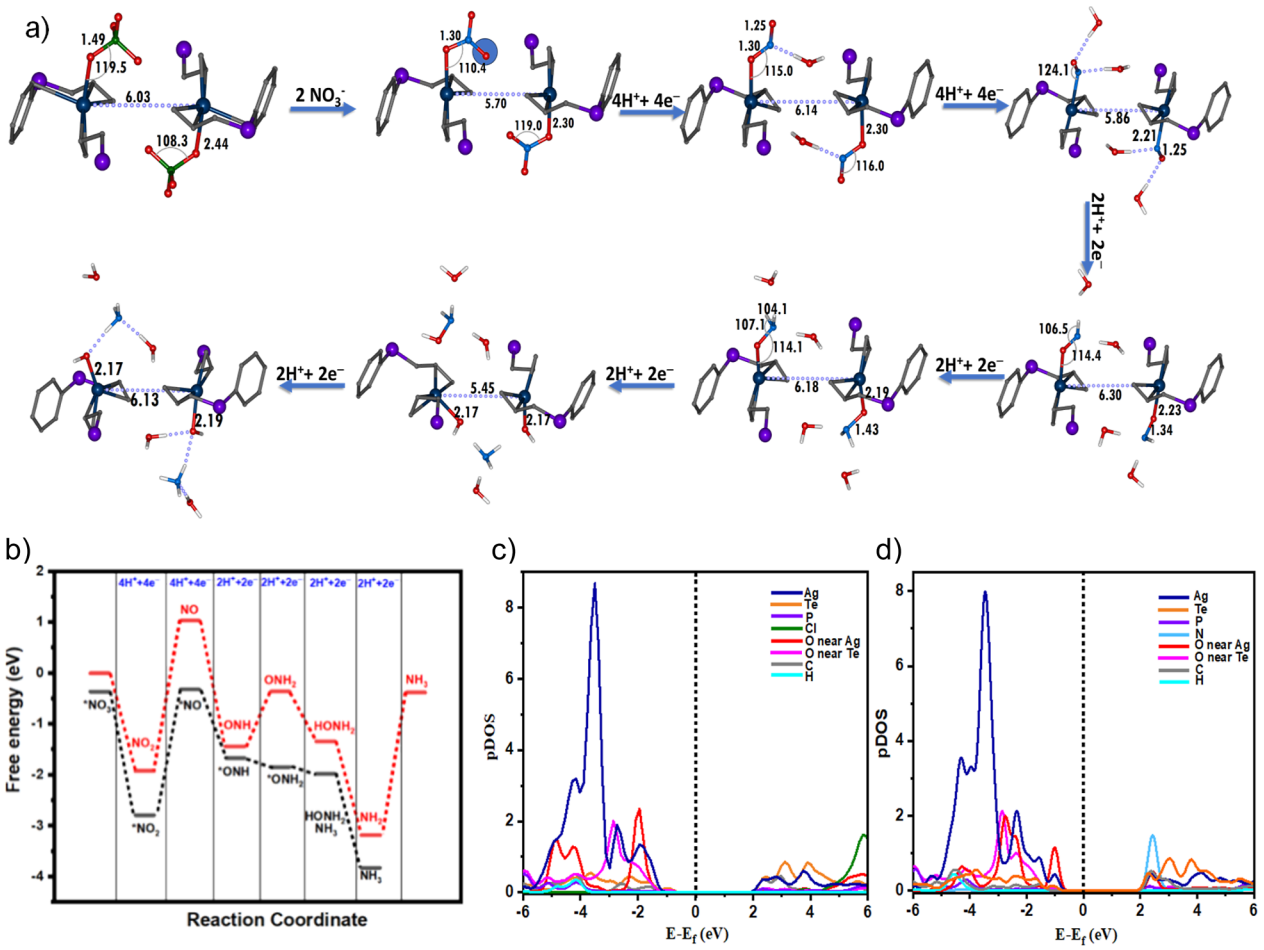

Figure 4. (a) DFT-optimized geometries of various reaction intermediates along the conversion of NO_3^- to NH_3, (b) potential energy surface computed with entropy corrections (black for Ag-TAM and red for TAM) (for those without entropy corrections, check Figure S44), (c) pDOS plot of Ag-TAM-ClO_4^-, and (d) pDOS plot of Ag-TAM-NO_3^-.

singlet at δ 28.7 ppm, a slight downfield shift to that of TAM (Figure S17). The bulk purity of Ag-TAM was confirmed by PXRD, which correlated well with the simulated pattern (Figure S18). The thermal stability was investigated through TGA, which showed Ag-TAM to be stable up to 200 °C, similar to TAM (Figure S19). FESEM images collected after grinding the crystals revealed that the morphologies of TAM and Ag-TAM are quite similar (Figures S8 and S21). The elemental mapping showed Ag to be distributed across Ag-TAM as expected (Figures 2d and S24). The ICP-OES analysis showed the composition of Ag, Te, and P to be of 3.1, 22.7, and 3.2%, respectively (Table S4). The insight about the surface composition of the Ag-TAM material was investigated by employing XPS analysis, as shown in Figure S25. The survey spectrum (Figure S25a) shows the presence of all of the elements in the material. In Figure S25b, Ag 3d spectra were deconvoluted into two peaks centered at 368.2 and 374.2 eV attributed to $3d_{5/2}$ and $3d_{3/2}$, representing the Ag + 1 oxidation state, and the peak at 366.9 eV is attributed to the Ag−C bond.[66,67] Additionally, bond valence sum calculation was performed, which also confirmed that Ag exists in the +1 oxidation state.[68] Ag-TAM proved to be sensitive to light due to the presence of Ag, which resulted in a color change from white to black in a span of 4-5 days with continuous exposure (Figure S26). This is the first time a cluster-based hybrid material has been produced by silver-π or metal-π interaction which is diverse from the conventional strategies, as mentioned in the Introduction. This could possibly improve the electron-transfer ability as these interactions are known to improve conductivity.[69]

Electrochemical Reduction of Nitrate to Ammonia. We sought to investigate the applicability of TAM and Ag-TAM as electrocatalysts for the reduction of nitrate to ammonia. ERNA was evaluated in an H-cell using 0.5 M Na_2SO_4 as an electrolyte with the catalyst deposited on carbon paper (CP) as the working electrode, platinum (Pt) wire as the counter electrode, and Ag/AgCl as the reference electrode. Before the ERNA test, LSV was performed. The reactant and reductive products, including nitrate, nitrite, and ammonia, were quantified by colorimetric methods.

TAM and Ag-TAM showed an increase in current density with the addition of NO_3^-, with Ag-TAM showing a much more significant response (Figure 3a). For TAM, the conversion of NO_3^- to NH_3 gradually increased from −0.88 to −1.28 V vs RHE with the faradaic efficiency, which is represented by a volcanic shape curve giving a maximum value of 84.7% at −1.18 V vs RHE (Figure S30). Now, we compared the activity of Ag-TAM to that of TAM and wanted to explore if the interlinking improves the activity. Like TAM, Ag-TAM shows an increase in conversion of NO_3^- to NH_3 from −0.88 to −1.18 V vs RHE but slightly decreases at −1.28 V (Figure 3b), probably due to the competitive hydrogen evolution

https://doi.org/10.1021/acs.inorgchem.4c02578
Inorg. Chem. 2024, 63, 21670−21678

reaction (HER).[16] Ag-TAM shows a 2-fold increase in the NH_3 yield rate compared to TAM, which is quite significant, and it also records a very high faradaic efficiency of 94.6% at −1.18 V vs RHE (Figure 3c). In both cases, NO_2^- was detected (Figures S32 and S33). For Ag-TAM, a maximum selectivity value of 79.2% was observed for NH_3 at −1.18 V, which was significantly better than 60% shown by TAM (Figure S34). As Ag-TAM showed better activity than TAM, we conducted further experiments on Ag-TAM at an operation voltage of −1.18 V vs RHE. After eight consecutive cycles, Ag-TAM upheld NH_3 yield rate and faradaic efficiency fairly, indicating that Ag-TAM

has excellent long-term catalytic stability (Figure 3d). Meanwhile, we also tested the stability for a period of 100 h, and there was no decrease in the current density (Figure S36). The morphology of the Ag-TAM poststability test was established by FESEM and the EDAX analysis, confirming the presence of Ag-TAM on the carbon paper (Figures S37 and S38). To confirm that the NH_3 produced is from NO_3^- being added, we performed a $^{15}NO_3^-$ isotope labeling experiment. The ^1H NMR spectra revealed a triplet when $^{14}NO_3^-$ was used, corresponding to $^{14}NH_4^+$, and when $^{15}NO_3^-$ was used, a doublet was observed, characteristic of $^{15}NH_4^+$ (Figure 3e). Ag-TAM showed comparable or better activity than the previously reported ERNA catalysts. To understand the activity of TAM and Ag-TAM, electrochemical impedance spectra were measured. The Nyquist plot showed that Ag-TAM has a smaller charge-transfer resistance (R_{ct}) than that of TAM, and values fitted by the equivalent circuit are 15.36 and 10.6 Ω for TAM and Ag-TAM, respectively (Figure 3f). The improvement in R_{ct} for Ag-TAM is mainly ascribed to the macrocycle being interlinked via silver-π interaction as this would improve the electron-transfer ability. In addition, we assessed the electrochemical active surface areas (ECSAs) of TAM and Ag-TAM by the electrochemical double-layer capacitance method. Ag-TAM showed a specific capacitance of 394.5 $\mu F\ cm^{-2}$, while TAM showed 173.4 $\mu F\ cm^{-2}$, demonstrating that Ag-TAM provides more active sites for nitrate reduction (Figures S40 and S41).

DFT Study. To understand the mechanism of this intriguing transformation, we have performed periodic DFT calculations using the VASP suite[70] (see ESI for computational details). This is carried out with the aim to uncover the reasons behind the remarkable efficacy exhibited by Ag-TAM in nitrate reduction. The mechanism adapted for NO_3^- to NH_3 conversion is shown in Figure S43 in Supporting Information. The snapshot of the active site corresponding to each intermediate along the transformation and the computed potential energy surface are shown in Figure 4a,b. The comprehensive reaction involves successive deoxygenation (Ag-TAM-NO_3 →Ag-TAM-NO_2 →Ag-TAM-NO) and hydrogenation (Ag-TAM-ONH →Ag-TAM-ONH_2 → NH_2OH → NH_3) steps. The consistently descending energy profile confirms that the reaction is an exergonic process (ΔG <0), underscoring its thermodynamic favorability and ease of occurrence. In the initial stage, a nucleophilic substitution occurs, wherein NO_3^- ions replace the ClO_4^- ion coordinated. This step is exothermic in nature (−0.36 eV), indicative of a favorable substitution process. This strong coordination of NO_3^- in the place of ClO_4^- is due to stronger donation, and this is exemplified in the partial density of states (pDOS) plot (Figure 4c,d). Particularly, the pDOS plot suggests that the charge transfer from NO_3^- to Ag occurs dominantly to the $4d_{z^2}$ orbitals of the silver (Figure S45). Furthermore, the pDOS analysis of Ag-TAM-NO_3 indicates a potential interaction between Te and NO_3^-. Upon comparison of the pDOS analysis of Ag-TAM-NO_3 with that of TAM-NO_3, it is clear that the density corresponding to the Ag ions and the nitrate anions is much closer (0.0008 eV) in energy, enabling favorable overlap and stronger interaction (Figure S46). For TAM, on the other hand, the density corresponding to Te is further down in the valence band, enhancing the gap between Te and the nitrate anion (0.1 eV). This leads to weaker binding and lower efficiency, as seen experimentally. This interaction provides an explanation for the experimental observation of NO_3^- conversion to NH_3 in TAM, albeit with lower efficiency.

After the binding of NO_3^- to Ag, there are two terminal oxygen centers that could be subjected to attack by the protons. To unveil the favorable active site, Bader charge analysis was performed, which revealed that O^1 (highlighted by a blue circle in Figure 4a) had a greater negative charge compared to O^2 (−0.58 vs −0.52). The addition of two protons and two electrons to O^1 is found to be favorable and results in the exothermic conversion (−2.79 eV) of Ag-TAM-ONO_2 to Ag-TAM-ONO. In the next step, two protons and electrons are added to the bound Ag-TAM-ONO group, which resulted in two types of intermediates, one with Ag-TAM-NO binding mode and the other with Ag-TAM-ON binding mode, with the former being more favorable energetically. Further, another N−O bond is broken, and the step is exothermic by −0.31 eV from the reactant. In the next step, Ag-TAM-NO undergoes a hydrogenation process leading to the formation of the Ag-TAM-ONH species, which is exothermic (−1.66 eV). Further hydrogenation leads to the formation of Ag-TAM-ONH_2 (−1.84 eV). In the next step, hydrogenation is assumed to lead to the expected formation of Ag-TAM-NH_2OH on both silver sites in the asymmetric unit. Quite interestingly, at this step, in one of the Ag active sites, the water present was found to donate a proton to the NH_2OH group, converting it to NH_3, and the OH^- thus produced from this donation was found to bind to the next silver ion (see Figure 4a). The strong binding of OH with Ag results in a weakening of its bond with the NH_2OH group. This indicates cooperative catalysis occurring within the hybrid material, elucidating the necessity for such extended materials to facilitate such efficient transformations. This step is exothermic (−1.98 eV) with one NH_3 already produced and one NH_2OH bound weakly to Ag. Finally, further hydrogenation leads to the release of two molecules of NH_3 and the regeneration of the catalyst, and this step is also exothermic by −3.85 eV. To substantiate that the efficiency of the NO_3^- to NH_3 conversion is indeed lower in TAM, we conducted a similar mechanistic study. We found that the rate-determining step, the conversion from NO_2^- to NO, is highly endothermic (+1.02 eV), as illustrated in Figure 4b (red profile), proving its lower efficiency than that of Ag-TAM. Additionally, we evaluated the possibility of the competing HER while investigating the nitrate reduction reaction. Our findings indicate that HER is highly endothermic in nature (Figures S47 and S48). Ag-TAM shows better or comparable ERNA when equated with various literature reports (Table S6). Moreover, when it is compared to silver-based systems,[22] it shows better activity. The ammonia being produced from nitrate reduction can be retrieved by standard literature procedures.[71,72]

https://doi.org/10.1021/acs.inorgchem.4c02578
Inorg. Chem. 2024, 63, 21670−21678

CONCLUSIONS

In summary, we present a functionalized 12-membered tellurium macrocycle, TAM, which acts as a molecular building block. Using TAM, we synthesized a novel 1D crystalline hybrid material, Ag-TAM, which is an interlinked macrocycle built via silver-π interaction. This is an unconventional approach to producing an interlinked cluster-based hybrid material. To further demonstrate the applicability of these systems, we investigated their ability to act as electrocatalysts for the reduction of nitrate to ammonia. TAM and Ag-TAM showed ERNA capability, which is the first time for organotellurium-based compounds, with Ag-TAM showing enhancement of its activity with a high FE of 94.6%. A comprehensive theoretical study based on periodic DFT calculations reveals novel mechanistic insights and suggests the presence of possible cooperative catalysis between the neighboring Ag sites. These findings elucidate the underlying factors responsible for greater efficiency in the catalytic process and show that interlinking and the presence of silver play roles in improving its activity. This work provides a new approach to explore the organometallic−inorganic hybrid material area. There is plenty of scope for expanding these systems into 2D and 3D arrays while also employing different metals to interlink, which will be fascinating.

ASSOCIATED CONTENT

Supporting Information

The Supporting Information is available free of charge at https://pubs.acs.org/doi/10.1021/acs.inorgchem.4c02578.

Additional experimental details, computational details, including additional characterization data like NMR, PXRD, TGA, and FESEM image (PDF)

Accession Codes

CCDC 2330481 and 2330484 contain the supplementary crystallographic data for this paper. These data can be obtained free of charge via www.ccdc.cam.ac.uk/data_request/cif, or by emailing data_request@ccdc.cam.ac.uk, or by contacting The Cambridge Crystallographic Data Centre, 12 Union Road, Cambridge CB2 1EZ, UK; fax: +44 1223 336033.

AUTHOR INFORMATION

Corresponding Authors

Gopalan Rajaraman − *Department of Chemistry, Indian Institute of Technology Bombay, Powai, Mumbai 400076, India*; orcid.org/0000-0001-6133-3026; Email: rajaraman@chem.iitb.ac.in

Viswanathan Baskar − *School of Chemistry, University of Hyderabad, Hyderabad 500046, India*; orcid.org/0000-0002-5270-3272; Email: vbsc@uohyd.ac.in

Authors

Calvin Samuel − *School of Chemistry, University of Hyderabad, Hyderabad 500046, India*; orcid.org/0000-0003-1528-9284

Gujju Narsimhulu − *School of Chemistry, University of Hyderabad, Hyderabad 500046, India*; orcid.org/0000-0001-5282-0770

Garima Bangar − *Department of Chemistry, Indian Institute of Technology Bombay, Powai, Mumbai 400076, India*

Sai Hemanth Kumar Dasari − *School of Chemistry, University of Hyderabad, Hyderabad 500046, India*; orcid.org/0000-0003-1407-3158

Complete contact information is available at: https://pubs.acs.org/10.1021/acs.inorgchem.4c02578

Author Contributions

C.S. and G.N. performed the research. G.B. performed the DFT calculation. S.H.K.D. helped with electrochemical studies. G.R. analyzed the DFT data. V.B. designed and conceptualized the research.

Funding

We thank SERB for funding (CRG/2023/000684).

Notes

The authors declare no competing financial interest.

ACKNOWLEDGMENTS

We thank SERB for funding (CRG/2023/000684).

ABBREVIATIONS

TAM, tellurium allyl macrocycle;; ERNA, electrochemical reduction of nitrate to ammonia;; SCXRD, single-crystal X-ray diffraction;; ESI-MS, electrospray ionization mass spectrometry;; FE, faradaic efficiency;; pDOS, partial density of states.

REFERENCES

(1) Wu, Z.-Y.; Karamad, M.; Yong, X.; Huang, Q.; Cullen, D. A.; Zhu, P.; Xia, C.; Xiao, Q.; Shakouri, M.; Chen, F.-Y.; Kim, J. Y. T.; Xia, Y.; Heck, K.; Hu, Y.; Wong, M. S.; Li, Q.; Gates, I.; Siahrostami, S.; Wang, H. Electrochemical ammonia synthesis via nitrate reduction on Fe single atom catalyst. *Nat. Commun.* **2021**, *12*, 2870.

(2) Lin, Y.-X.; Zhang, S.-N.; Xue, Z.-H.; Zhang, J.-J.; Su, H.; Zhao, T.-J.; Zhai, G.-Y.; Li, X.-H.; Antonietti, M.; Chen, J.-S. Boosting selective nitrogen reduction to ammonia on electron-deficient copper nanoparticles. *Nat. Commun.* **2019**, *10*, 4380.

(3) Chanda, D.; Xing, R.; Xu, T.; Liu, Q.; Luo, Y.; Liu, S.; Tufa, R. A.; Dolla, T. H.; Montini, T.; Sun, X. Electrochemical nitrogen reduction: recent progress and prospects. *Chem. Commun.* **2021**, *57*, 7335−7349.

(4) Li, J.; Zhan, G.; Yang, J.; Quan, F.; Mao, C.; Liu, Y.; Wang, B.; Lei, F.; Li, L.; Chan, A. W. M.; Xu, L.; Shi, Y.; Du, Y.; Hao, W.; Wong, P. K.; Wang, J.; Dou, S.-X.; Zhang, L.; Yu, J. C. Efficient Ammonia Electrosynthesis from Nitrate on Strained Ruthenium Nanoclusters. *J. Am. Chem. Soc.* **2020**, *142*, 7036−7046.

(5) Wang, Y.; Xu, A.; Wang, Z.; Huang, L.; Li, J.; Li, F.; Wicks, J.; Luo, M.; Nam, D.-H.; Tan, C.-S.; Ding, Y.; Wu, J.; Lum, Y.; Dinh, C.-T.; Sinton, D.; Zheng, G.; Sargent, E. H. Enhanced Nitrate-to-Ammonia Activity on Copper−Nickel Alloys via Tuning of Intermediate Adsorption. *J. Am. Chem. Soc.* **2020**, *142*, 5702−5708.

(6) Wang, Y.; Zhou, W.; Jia, R.; Yu, Y.; Zhang, B. Unveiling the Activity Origin of a Copper-based Electrocatalyst for Selective Nitrate Reduction to Ammonia. *Angew. Chem., Int. Ed.* **2020**, *59*, 5350−5354.

(7) Liu, Z.; Wang, C.; Chen, C.; Li, C.; Guo, C. Selective electroreduction of nitrate to ammonia with high Faradaic efficiency on nanocrystalline silver. *Electrochem. Commun.* **2021**, *131*, 107121.

(8) Xu, Y.; Ren, K.; Ren, T.; Wang, M.; Liu, M.; Wang, Z.; Li, X.; Wang, L.; Wang, H. Cooperativity of Cu and Pd active sites in CuPd aerogels enhances nitrate electroreduction to ammonia. *Chem. Commun.* **2021**, *57*, 7525−7528.

(9) Zhang, G.; Wang, F.; Chen, K.; Kang, J.; Chu, K. Atomically Dispersed Sn Confined in FeS_2 for Nitrate-to-Ammonia Electroreduction. *Adv. Funct. Mater.* **2024**, *34*, 2305372.

(10) Guo, Y.; Zhang, R.; Zhang, S.; Zhao, Y.; Yang, Q.; Huang, Z.; Dong, B.; Zhi, C. Pd doping-weakened intermediate adsorption to promote electrocatalytic nitrate reduction on TiO_2 nanoarrays for ammonia production and energy supply with zinc-nitrate batteries. *Energy Environ. Sci.* **2021**, *14*, 3938−3944.

(11) Zhang, R.; Li, C.; Cui, H.; Wang, Y.; Zhang, S.; Li, P.; Hou, Y.; Guo, Y.; Liang, G.; Huang, Z.; Peng, C.; Zhi, C. Electrochemical

nitrate reduction in acid enables high-efficiency ammonia synthesis and high-voltage pollutes-based fuel cells. *Nat. Commun.* **2023**, *14*, 8036.
(12) Yin, H.; Peng, Y.; Li, J. Electrocatalytic Reduction of Nitrate to Ammonia via a Au/Cu Single Atom Alloy Catalyst. *Environ. Sci. Technol.* **2023**, *57*, 3134−3144.
(13) Chen, G.-F.; Yuan, Y.; Jiang, H.; Ren, S. Y.; Ding, L.-X.; Ma, L.; Wu, T.; Lu, J.; Wang, H. Electrochemical reduction of nitrate to ammonia via direct eight-electron transfer using a copper-molecular solid catalyst. *Nat. Energy* **2020**, *5*, 605−613.
(14) Jia, R.; Wang, Y.; Wang, C.; Ling, Y.; Yu, Y.; Zhang, B. Boosting Selective Nitrate Electroreduction to Ammonium by Constructing Oxygen Vacancies in TiO_2. *ACS Catal.* **2020**, *10*, 3533−3540.
(15) Liu, L.; Zheng, S.-J.; Chen, H.; Cai, J.; Zang, S.-Q. Tandem Nitrate-to-Ammonia Conversion on Atomically Precise Silver Nanocluster/Mxene Electrocatalyst. *Angew. Chem., Int. Ed.* **2024**, *63*, No. e202316910.
(16) Zhang, G.; Li, X.; Chen, K.; Guo, Y.; Ma, D.; Chu, K. Tandem Electrocatalytic Nitrate Reduction to Ammonia on Mbenes. *Angew. Chem., Int. Ed.* **2023**, *62*, No. e202300054.
(17) Zhang, N.; Wan, Y.; Chen, K.; Zhang, G.; Chu, K. P-d hybridized In-Co dual sites promote nitrite electroreduction to ammonia at high current density. *Nano Energy* **2024**, *125*, 109594.
(18) Chen, K.; Wang, G.; Guo, Y.; Ma, D.; Chu, K. Iridium single-atom catalyst for highly efficient NO electroreduction to NH_3. *Nano Res.* **2023**, *16*, 8737−8742.
(19) Lv, F.; Sun, M.; Hu, Y.; Xu, J.; Huang, W.; Han, N.; Huang, B.; Li, Y. Near-unity electrochemical conversion of nitrate to ammonia on crystalline nickel porphyrin-based covalent organic frameworks. *Energy Environ. Sci.* **2023**, *16*, 201−209.
(20) Hu, H.; Miao, R.; Yang, F.; Duan, F.; Zhu, H.; Hu, Y.; Du, M.; Lu, S. Intrinsic Activity of Metalized Porphyrin-based Covalent Organic Frameworks for Electrocatalytic Nitrate Reduction. *Adv. Energy Mater.* **2024**, *14*, 2302608.
(21) Gao, Z.; Lai, Y.; Tao, Y.; Xiao, L.; Zhang, L.; Luo, F. Constructing Well-Defined and Robust Th-MOF-Supported Single-Site Copper for Production and Storage of Ammonia from Electroreduction of Nitrate. *ACS Cent. Sci.* **2021**, *7*, 1066−1072.
(22) Chu, J.; Liu, Z.; Jiang, L.; Cai, F.; Sun, C.; Kong, A.; Ding, H. Coordination polymers-derived core-shell Co@N−C nanostructures as efficient dual functional catalysts for nitrate electroreduction and Fenton-like catalytic dye degradation. *J. Solid State Chem.* **2022**, *315*, 123485.
(23) Zhang, Y.; Zheng, H.; Zhou, K.; Ye, J.; Chu, K.; Zhou, Z.; Zhang, L.; Liu, T. Conjugated Coordination Polymer as a New Platform for Efficient and Selective Electroreduction of Nitrate into Ammonia. *Adv. Mater.* **2023**, *35*, 2209855.
(24) Wang, Y.-M.; Cai, J.; Wang, Q.-Y.; Li, Y.; Han, Z.; Li, S.; Gong, C.-H.; Wang, S.; Zang, S.-Q.; Mak, T. C. W. Electropolymerization of Metal Clusters Establishing a Versatile Platform for Enhanced Catalysis Performance. *Angew. Chem., Int. Ed.* **2022**, *61*, No. e202114538.
(25) Kickelbick, G. Hybrid Materials − Past, Present and Future. *Hybrid Mater.* **2014**, *1*, 39−51.
(26) Schubert, U. Cluster-based inorganic-organic hybrid materials. *Chem. Soc. Rev.* **2011**, *40*, 575−582.
(27) Attenberger, B.; Welsch, S.; Zabel, M.; Peresypkina, E.; Scheer, M. Diphosphorus Complexes as Building Blocks for the Design of Phosphorus-Containing Organometallic-Organic Hybrid Materials. *Angew. Chem., Int. Ed.* **2011**, *50*, 11516−11519.
(28) Attenberger, B.; Peresypkina, E. V.; Scheer, M. Novel Two- and Three-Dimensional Organometallic-Organic Hybrid Materials Based on Polyphosphorus Complexes. *Inorg. Chem.* **2015**, *54*, 7021−7029.
(29) Shelyganov, P. A.; Elsayed Moussa, M.; Seidl, M.; Scheer, M. Organometallic-Organic Hybrid Assemblies Featuring the Diantimony Complex $[Cp_2Mo_2(CO)_4(\mu,\eta^2\text{-}Sb_2)]$, Ag^I Ions and N-Donor Molecules as Building Blocks. *Chem.—Eur. J.* **2023**, *29*, No. e202300610.
(30) Anwander, R. S. O. M. C. @P. M. S. SOMC@PMS. Surface Organometallic Chemistry at Periodic Mesoporous Silica. *Chem. Mater.* **2001**, *13*, 4419−4438.
(31) Maishal, T. K.; Alauzun, J.; Basset, J.-M.; Copéret, C.; Corriu, R. J. P.; Jeanneau, E.; Mehdi, A.; Reyé, C.; Veyre, L.; Thieuleux, C. A Tailored Organometallic−Inorganic Hybrid Mesostructured Material: A Route to a Well-Defined, Active, and Reusable Heterogeneous Iridium-NHC Catalyst for H/D Exchange. *Angew. Chem., Int. Ed.* **2008**, *47*, 8654−8656.
(32) Guo, C.; Li, M.; Chen, J.; Luo, Y. Highly selective redistribution of primary arylsilanes to secondary arylsilanes catalyzed by Ln-$(CH_2C_6H_4NMe_2\text{-}o)_3$@SBA-15. *Chem. Commun.* **2020**, *56*, 117−120.
(33) Chakraborty, D.; Nandi, S.; Maity, R.; Motkuri, R. K.; Han, K. S.; Collins, S.; Humble, P.; Hayes, J. C.; Woo, T. K.; Vaidhyanathan, R.; Thallapally, P. K. An Ultra-Microporous Metal-Organic Framework with Exceptional Xe Capacity. *Chem.—Eur. J.* **2020**, *26*, 12544−12548.
(34) Liu, J.; Strachan, D. M.; Thallapally, P. K. Enhanced noble gas adsorption in Ag@MOF-74Ni. *Chem. Commun.* **2014**, *50*, 466−468.
(35) Jo, Y.-M.; Jo, Y. K.; Lee, J.-H.; Jang, H. W.; Hwang, I.-S.; Yoo, D. J. MOF-Based Chemiresistive Gas Sensors: Toward New Functionalities (Adv. Mater. 43/2023). *Adv. Mater.* **2023**, *35*, 2206842.
(36) Yao, M.-S.; Xiu, J. W.; Huang, Q.-Q.; Li, W.-H.; Wu, W.-W.; Wu, A.-Q.; Cao, L.-A.; Deng, W.-H.; Wang, G.-E.; Xu, G. Van der Waals Heterostructured MOF-on-MOF Thin Films: Cascading Functionality to Realize Advanced Chemiresistive Sensing. *Angew. Chem., Int. Ed.* **2019**, *58*, 14915−14919.
(37) Cong, S.; Yuan, Y.; Wang, J.; Wang, Z.; Kapteijn, F.; Liu, X. Highly Water-Permeable Metal−Organic Framework MOF-303 Membranes for Desalination. *J. Am. Chem. Soc.* **2021**, *143*, 20055−20058.
(38) Li, L.; Chen, L.; Guo, L.; Zheng, F.; Zhang, Z.; Yang, Q.; Yang, Y.; Su, B.; Ren, Q.; Li, J.; Bao, Z. Supramolecular Assembly of One-Dimensional Coordination Polymers for Efficient Separation of Xenon and Krypton. *ACS Appl. Mater. Interfaces* **2023**, *15*, 41438−41446.
(39) Liu, G.; Yang, X.; Bonnefont, A.; Lv, Y.; Chen, J.; Dan, W.; Chen, Z.; Ruhlmann, L.; Wright, D. S.; Zhang, C. Conjugated hybrid films based on a new polyoxotitanate monomer. *Chem. Commun.* **2018**, *54*, 14132−14135.
(40) Hasegawa, S.; Horike, S.; Matsuda, R.; Furukawa, S.; Mochizuki, K.; Kinoshita, Y.; Kitagawa, S. Three-Dimensional Porous Coordination Polymer Functionalized with Amide Groups Based on tridentate Ligand: Selective Sorption and Catalysis. *J. Am. Chem. Soc.* **2007**, *129*, 2607−2614.
(41) Büschelberger, P.; Gärtner, D.; Reyes-Rodriguez, E.; Kreyenschmidt, F.; Koszinowski, K.; Jacobi von Wangelin, A.; Wolf, R. Alkene Metalates as Hydrogenation Catalysts. *Chem.—Eur. J.* **2017**, *23*, 3139−3151.
(42) Li, F.; Chen, X.; Huang, B.-Q.; Xu, H.-D.; Zhu, C.-F.; Shen, M.-H. Palladium-catalyzed ring-opening [5 + 2] annulation of vinylethylene carbonates (VECs) and C5-substituted Meldrum's acids: rapid synthesis of 7-membered lactones. *Chem. Commun.* **2024**, *60*, 1774−1777.
(43) Li, D.; Shen, C.; Si, Z.; Liu, L. Palladium-Catalyzed Fluorinative Bifunctionalization of Aziridines and Azetidines with gem-Difluorocyclopropanes. *Angew. Chem., Int. Ed.* **2023**, *135*, No. e202310283.
(44) Chen, B.-H.; Liu, S.-J.; Zhao, Q.; Hou, Q.; Yuan, J.-L.; Zhan, G.; Yang, Q.-Q.; Huang, W. Palladium-catalyzed asymmetric [4 + 2] annulation of vinyl benzoxazinanones with pyrazolone 4,5-diones to access spirobenzoxazine frameworks. *Chem. Commun.* **2023**, *59*, 1233−1236.
(45) Mispelaere-Canivet, C.; Spindler, J.-F.; Perrio, S.; Beslin, P. $Pd_2(dba)_3$/Xantphos-catalyzed cross-coupling of thiols and aryl bromides/triflates. *Tetrahedron* **2005**, *61*, 5253−5259.
(46) Kirchhoff, J. H.; Dai, C.; Fu, G. C. A Method for Palladium-Catalyzed Cross-Couplings of Sumple Alkyl Chlorides: Suzuki

https://doi.org/10.1021/acs.inorgchem.4c02578
Inorg. Chem. 2024, 63, 21670−21678

Reactions Catalyzed by $[Pd_2(dba)_3]/PCy_3$. *Angew. Chem., Int. Ed.* **2002**, *41*, 1945−1947.
(47) Zang, S.-Q.; Han, J.; Mak, T. C. W. Silver(I)-Organic Networks Assembled with the Flexible Prop-2-ynyloxybenzene Ligand: In Situ Recrystallization and Unusual Silver-Aromatic Interaction. *Organometallics* **2009**, *28*, 2677−2683.
(48) Layfield, R. A.; McDouall, J. J.; Sulway, S.; Tuna, F.; Collison, D.; Winpenny, R. E. P. Influence of the N-Bridging Ligand on Magnetic Relaxation in an Organometallic Dysprosium Single-Molecule Magnet. *Chem.—Eur. J.* **2010**, *16*, 4442−4446.
(49) Bernhardt, M.; Korzyński, M. D.; Berkson, Z.; Pointillart, F.; Le Guennic, B.; Cador, O.; Copéret, C. Tailored Lewis Acid Sites for High-Temperature Supported Single-Molecule Magnetism. *J. Am. Chem. Soc.* **2023**, *145*, 12446−12451.
(50) Guo, F.-S.; Day, B. M.; Chen, Y.-C.; Tong, M.-L.; Mansikkamäki, A.; Layfield, R. A. Magnetic hysteresis up to 80 kelvin in a dysprosium metallocene single-molecule magnet. *Science* **2018**, *362*, 1400−1403.
(51) Le Roy, J. J.; Jeletic, M.; Gorelsky, S. I.; Korobkov, I.; Ungur, L.; Chibotaru, L. F.; Murugesu, M. An Organometallic Building Block Approach To Produce a Multidecker 4*f* Single-Molecule Magnet. *J. Am. Chem. Soc.* **2013**, *135*, 3502−3510.
(52) De, S.; Mondal, A.; Ruan, Z.-Y.; Tong, M.-L.; Layfield, R. A. Dynamic Magnetic Properties of Germole-ligated Lanthanide Sandwich Complexes. *Chem.—Eur. J.* **2023**, *29*, No. e202300567.
(53) Zhang, P.; Luo, Q.-C.; Zhu, Z.; He, W.; Song, N.; Lv, J.; Wang, X.; Zhai, Q.-G.; Zheng, Y.-Z.; Tang, J. Radical-Bridged Heterometallic Single-Molecule Magnets Incorporating Four Lanthanoceniums. *Angew. Chem., Int. Ed.* **2023**, *135*, No. e202218540.
(54) Hatano, A.; Sugawa, T.; Mimura, R.; Kataoka, S.; Yamamoto, K.; Omoda, T.; Zhu, B.; Tian, Y.; Sakaki, S.; Murahashi, T. Isolation and Structures of Polyarene Palladium Nanoclusters. *J. Am. Chem. Soc.* **2023**, *145*, 15030−15035.
(55) Münzfeld, L.; Gillhuber, S.; Hauser, A.; Lebedkin, S.; Hädinger, P.; Knöfel, N. D.; Zovko, C.; Gamer, M. T.; Weigend, F.; Kappes, M. M.; Roesky, P. W. Synthesis and properties of cyclic sandwich compounds. *Nature* **2023**, *620*, 92−96.
(56) Inkpen, M. S.; Scheerer, S.; Linseis, M.; White, A. J. P.; Winter, R. F.; Albrecht, T.; Long, N. J. Oligomeric ferrocene rings. *Nat. Chem.* **2016**, *8*, 825−830.
(57) Srungavruksham, N. K.; Baskar, V. $Te_4Se_2O_6$ macrocycle stabilizing triangular planar and tetrahedral anions. *Dalton Trans.* **2015**, *44*, 4554−4559.
(58) Srungavruksham, N. K.; Baskar, V. 12-Membered Macrocycles Containing Ditelluroxane and Selenotelluroxane Units. *Eur. J. Inorg. Chem.* **2012**, *2012*, 136−142.
(59) Narsimhulu, G.; Samuel, C.; Palani, S.; Dasari, S. H. K.; Krishnamoorthy, K.; Baskar, V. Electrocatalytic hydrogen evolution mediated by an organotelluroxane macrocycle stabilized through secondary interactions. *Dalton Trans.* **2023**, *52*, 17242−17248.
(60) Dolomanov, O. V.; Bourhis, L. J.; Gildea, R. J.; Howard, J. A. K.; Puschmann, H. *OLEX2*: a complete structure solution, refinement and analysis program. *J. Appl. Crystallogr.* **2009**, *42*, 339−341.
(61) Sheldrick, G. M. *SHELXT* − Intergrated space-group and crystal-structure determination. *Acta Crystallogr.* **2015**, *A71*, 3−8.
(62) Sheldrick, G. M. Crystal structure refinement with *SHELXL*. *Acta Crystallogr.* **2015**, *71*, 3−8.
(63) Boyd, E. A.; Boyd, M. E. K.; Loh, Jr. V. M. Facile synthesis of functionalised phenylphosphinic acid derivatives. *Tetrahedron Lett.* **1996**, *37*, 1651−1654.
(64) Bergman, J. Tellurium in organic chemistry-I: A novel synthesis of biaryls. *Tetrahedron* **1972**, *28*, 3323−3331.
(65) Kolen, M.; Smith, W. A.; Mulder, F. M. Accelerating ^{1}H NMR Detection of Aqueous Ammonia. *ACS Omega* **2021**, *6*, 5698−5704.
(66) Ferraria, A. M.; Carapeto, A. P.; Botelho do Rego, A. M. X-ray photoelectron spectroscopy: Silver salts revisited. *Vacuum* **2012**, *86*, 1988−1991.
(67) Yang, D.-H.; Cao, X.-L.; Yang, L.; Zhou, Y.-L. Study on precipitates in $AgGaSe_2$ single crystal grown by vertical gradient freezing method. *Mater. Res. Express* **2020**, *7*, 125901.
(68) O'Keefe, M.; Brese, N. E. Atom sizes and bond lengths in molecules and crystals. *J. Am. Chem. Soc.* **1991**, *113*, 3226−3229.
(69) Song, Y.-J.; Ren, S.-Y.; Zuo, S.; Shi, Z.-Q.; Li, Z.; Li, G. Tailored Porous Ferrocene-Based Metal-Organic Frameworks as High-Performance Proton Conductors. *Inorg. Chem.* **2024**, *63*, 8194−8205.
(70) Hafner, J. *Ab-initio* simulations of materials using VASP: Density-functional theory and beyond. *J. Comput. Chem.* **2008**, *29*, 2044−2078.
(71) Shin, C.; Szczuka, A.; Liu, M. J.; Mendoza, L.; Jiang, R.; Tilmans, S. H.; Tarpeh, W. A.; Mitch, W. A.; Criddle, C. S. Recovery of Clean Water and Ammonia from Domestic Wastewater: Impacts on Embodied Energy and Greenhouse Gas Emissions. *Environ. Sci. Technol.* **2022**, *56*, 8712−8721.
(72) Wang, X.; Im, S.; Jung, B.; Wu, J.; Iddya, A.; Javier, Q.-R. A.; Xiao, M.; Ma, S.; Lu, S.; Jaewon, B.; Zhang, J.; Ren, Z. J.; Maravelias, C. T.; Hoek, E. M. V.; Jassby, D. Simple and Low-Cost Electroactive Membranes for Ammonia Recovery. *Environ. Sci. Technol.* **2023**, *57*, 9405−9415.

https://doi.org/10.1021/acs.inorgchem.4c02578
Inorg. Chem. 2024, 63, 21670−21678